G Ring Particle Sizes Derived from Ring Plane Crossing Observations

Henry B. Throop and Larry W. Esposito

Laboratory for Atmospheric and Space Physics, University of Colorado, Boulder, Colorado 80309-0392
E-mail: throop@colorado.edu

The Saturn ring plane crossings in 1995–1996 allowed observers using the Hubble Space Telescope and the W. M. Keck telescope to image the planet's diffuse rings from 0.3 to 2.2 μm at a scattering angle $\theta \sim 175°$. We calculate the G ring reflectance for size distributions of dust to kilometer-sized bodies derived from a physical, evolutionary model. The model tracks the evolution of the G ring from its initial formation following the disruption of a progenitor satellite (R. M. Canup and L. W. Esposito, 1997, Icarus 126, 28–41) until a steady state distribution is reached. We calculate the total particle scattering from contributions due to Mie scattering, isotropic scattering, and Lambert scattering and compare the spectra, phase curves, and RMS particle mass from our physical model to that observed by HST, Keck, and Voyager. A range of particle size distributions from the models are consistent with the observations. These distributions have a dust component that can be described by the differential power law exponent q_{dust}, in the range 1.5–3.5. A quasi-Gaussian size distribution centered at 15 μm also matches the observations, although is not predicted by the evolutionary model. Distributions with $q_{dust} \gtrsim 4$, such as that proposed by M. R. Showalter and J. N. Cuzzi (1993), Icarus 103, 124–143) based on Voyager G ring photometry, are too blue to match the spectrum. In order to fit the visible optical depth, many of the models require longer particle lifetimes against plasma drag than Voyager plasma measurements imply. This may suggest that plasma densities are overestimated, that the ring has unaccounted-for dust sources, or that the ring is not in steady-state and we are seeing it at a particularly bright moment. © 1998 Academic Press

Key Words: planetary rings; planetary rings, Saturn; regoliths; ices.

I. OVERVIEW

Twice during its 29-year orbital period, the ring plane of Saturn enters a period where it is oriented nearly edge-on to the Earth. In this viewing geometry, the planet's G ring—usually far too faint in the glare of the main rings to be detected from Earth—brightens substantially due to the increased line-of-sight particle abundance. During the 1995–1996 ring plane crossing (RPX) period, the ring plane passed through the exact edge-on orientation to the Earth three times, on 22 May 1995, 10 August 1995, and 11 February 1996, and passed through the Sun's plane on 19 November 1995. Observers using the Hubble Space Telescope (Nicholson *et al.* 1996) during the August and November events and the W. M. Keck 10-m telescope (de Pater *et al.* 1996) during the May and August events were successful in detecting the G ring from Earth—an observation that was considered unlikely only recently (Showalter and Cuzzi 1993). Observations of the G ring during four orbits using the HST Wide Field/Planetary Camera (WFPC2) yielded a spectrum from 0.3 to 0.89 μm at 5 wavelengths, while Keck imaged the ring at 2.26 μm. Observations of the ring were also made by observers at the Infrared Telescope Facility (Bauer *et al.* 1997) at 2.2 μm during the August event, and by observers using the Hubble Space Telescope (French *et al.* 1997) in October 1996, several months after the RPX events. This set of observations represents the first new data from the G ring in nearly 15 years and the first spectrally resolved observations of the ring. In this paper, we interpret the reflectance of the ring as being from a size distribution of small ice particles, develop a light scattering model for these particles, and find several classes of particle size distributions—some derived from physical models of the ring—that can explain the observed spectrum. Our models are constrained by observations (Table I) of the spectrum, the Voyager phase curve (Showalter and Cuzzi 1993), the RMS particle mass (Tsintikidis *et al.* 1994), and the charged-particle absorption signature of the ring (Hood 1989), as well as relevant laboratory light-scattering and impact experiments.

II. OBSERVATIONS AND PREVIOUS ANALYSIS

The G ring was first detected in 1979 by absorption of 100-MeV charged particles measured by Pioneer 11 as the spacecraft flew near the ring; initially, the absorption signature was ascribed to the satellite Janus. Voyager 1 detected the ring visually in 1980 and returned one clear

TABLE I
Summary of G Ring Observations

Year of observation		Analysis result	Reference(s)
1995–1996 Ring plane crossing	HST, Keck, IRTF, CFHT 0.3–2.26 μm spectra	Dust particle size distribution (this work)	Nicholson *et al.* 1996, de Pater *et al.* 1996, Bauer *et al.* 1996, French *et al.* 1997
1981	Voyager 2 *in situ* particle sampling	Particle size ~1–15 μm	Tsintkidis *et al.* 1994, Meyer-Vernet *et al.* 1997
1980–1981	Voyager 1 and 2 V-band photometry, phase curve	Optical depth dominated by sub-μm particles	Showalter and Cuzzi 1993
1979	Pioneer 11 proton absorption	Parent body cross section ~10–40 km^2	Hood 1989

image of the ring; in 1981 Voyager 2 returned one additional image. Showalter and Cuzzi (1993) later showed that Voyager 2 flew through the outer edge of the ring, and data from the plasma wave antennas at this crossing have subsequently been associated with direct ring particle impacts with the spacecraft (Aubier *et al.* 1983, Gurnett *et al.* 1983, Tsintkidis *et al.* 1994).

The recent observations differ from those of Voyager in that the recent ones are nearly in backscatter (scattering angle $\theta_{Aug} = 176.4°$; $\theta_{Nov} = 174.5°$; $\theta_{May} = 174.4°$) at five wavelengths (broad filters at $\lambda = 300, 450, 555, 675$ nm, and narrowband methane at 890 nm), while the Voyager images are mostly in forward scatter, $\theta = 30$–$60°$, through one broadband visual filter centered at $\lambda = 500$ nm. Showalter and Cuzzi (1993) detected faint signatures of the ring in 11 Voyager images in addition to two clearly visible images. The former images were subject to substantial processing, including frame coaddition and a polynomial background subtraction. The wide, diffuse E ring partially obscured the August edge-on G ring images; these images were processed to remove the contribution from the E ring.

Observations by French *et al.* (1997) consisted of a single HST image at $\lambda = 400$ μm and scattering angle $\theta = 178.1°$. This observation was significantly later than the RPX events and thus had a comparably large 3.8° ring opening angle, allowing for a measurement of the radial profile.

The first in-depth analysis of Voyager G ring photometry (Showalter and Cuzzi 1993, hereafter SC93) described it as a dusty "ghost" ring of V-band optical depth $\tau \sim 10^{-6}$, lying at an orbital radius a between 166,000 and 173,000 km (2.72–2.85 R_S), beyond the bright B and A rings and just inside the E ring. SC93 compared G ring observations at four scattering angles to phase functions predicted for several ring particle size distributions using Mie theory. They found the observations to be consistent with the phase function of contaminated ice particles in the range $r = 0.03$–40 μm, with a size distribution described by a power law,

$$n(r)\, dr = r^{-q_{dust}}\, dr, \qquad (1)$$

with an unusually high exponent $q_{dust} \simeq 6$ (a "steep distribution"). With this distribution, the majority of the ring's cross section is in small particles, which have extremely short lifetimes against drag forces in the ring; SC93 calculated a lifetime of 8–800 years for 1-μm particles. Because of the statistical unlikelihood of observing such a short-lived ring, SC93 proposed the ring to be sustained by a small number of "parent bodies" of $r \sim 1$ km, similar to models proposed for the Uranus and Neptune rings (e.g., Esposito and Colwell 1989, Colwell and Esposito 1990). In the parent body model, large bodies sustain the ring by providing a dust source to balance the loss by various processes. Reanalysis of the Pioneer absorption data (Hood 1989) has been interpreted to indicate a parent body geometric cross-section of 10–40 km^2 in a narrow band $\Delta a \sim 1000$ km across. SC93 proposed that these parent bodies were the remnants of a catastrophically fragmented saturnian satellite. The kilometer-sized parent bodies have a total optical depth $\tau_{par} \sim 10^{-8}$ and are too small to be directly visible in any current images.

Canup and Esposito (1997, hereafter CE97) developed a physical model of the G ring that describes the evolution of the ring particle size distribution from the breakup of a saturnian satellite, until loss and production of free dust particles in the ring approached steady-state. They constrained their model to match the SC93 normal optical depth and the Hood (1989) parent body cross section. A third constraint—which SC93 did not have at the time of their study—was the root-mean-square particle mass m_{rms} from the Tsintkidis *et al.* (1994) reanalysis of the Voyager 2 *in situ* particle sampling detected by the plasma wave spectrometer and planetary radio astronomy instruments (PWS/PRA). Tsintkidis *et al.* (1994) found $m_{rms} \sim 1.8 \times 10^{-8\pm1}$ g, or $r_{rms} \sim 16$ μm, for particles larger than the PWS/PRA detection limit of $\sim 5.4 \times 10^{-9}$ g. With these three constraints, CE97 predicted the slope of the G ring

dust to be $2.5 < q_{dust} < 4.5$ for the smallest particles, and were unable to match the observations with $q_{dust} \sim 6$ found by SC93.

The CE97 model matched the bulk optical depth of the ring, but did not attempt to match spectral or phase observations of the ring. Their light scattering calculations considered only the physical cross section of particles and did not use Mie or other more accurate scattering methods. The curent work expands on that of CE97 by considering the complete set of G ring observations, including new spectral and phase observations, and by using a more complete light scattering model.

III. G RING MODEL

In this paper, we adopt the CE97 G ring physical model. This model considers particles in the size range $r = 0.03$ μm–10 km. The distribution is stored in two state vectors divided into discrete size bins, one vector which includes only particles in the free state (i.e., single particles which contribute to ring optical depth and are not accreted to parent bodies), and one which includes both particles in the free state and those contained in parent body regoliths. The ring is assumed to be both radially and azimuthally homogeneous. At each time step, the number of particles added to the system, lost from the system, and moving between bins is calculated, and the state vectors updated. The simulation ends when a near-steady-state free particle distribution has been achieved, typically in $\lesssim 10^5$ years; at this point, loss and production of dust are nearly equalized. The subsequent lifetime of the parent bodies against catastrophic fragmentation is $\sim 10^8$ years, significantly shorter than the $\sim 10^{11}$-year time scale against steady meteoroid erosion (SC93).

The processes considered by the CE97 model are (i) dust *production* into the free state by meteoroid flux into parent body regoliths and mutual collisions between parent bodies and (ii) dust *loss* from the free state by parent body sweep-up, destructive meteoroid impacts, and plasma and Poynting–Robertson drag forces. Three-body accretion criteria in the Roche zone (Canup and Esposito 1995) are used to calculate the size distribution of the parent bodies; typical distributions are 5–15 bodies of 0.1–1 km. A description of the CE97 model parameters that we consider in this study is presented in Table II; we refer the reader to CE97 for a complete description of their model.

Both our work and that of CE97 consider only the processes occurring in the core ($\Delta a \sim 1000$ km) of the ring. After small particles are removed outward from the core they continue to drift outward but do not interact with the parent bodies. However, the ring profile is observed to be broadly symmetric inward and outward from the central core (SC93), suggesting that dust particles on eccentric orbits dominate the radial profile. Therefore, we assume

that the entire brightness of the ring is due to particles currently interacting with the central core, and do not consider those swept out of the core. In a future work we will consider the complete radial profile of the ring.

Dust Production Processes

Mass yields from meteoroid impacts into parent bodies are calculated using the meteoroid flux models described in Colwell and Esposito (1990) and the surface yield parameterizations of Greenberg *et al.* (1978). We make one significant change to the CE97 model in calculating the size range of regolith ejecta from micrometeoroid impacts. Their model assumes that the ejecta from each micrometeoroid impact is distributed in a power law of slope q_{ej}, with lower size cutoff $r_{min} = 0.03$ μm. The upper size cutoff is set such that exactly one particle exists larger than the largest size in their distribution; i.e.,

$$N_{r > r_{max}} \equiv 1. \tag{2}$$

The $n(r)$ ejecta distribution from each impact is then determined by setting the total mass ejected,

$$m_{ej} = \tfrac{1}{2} m_{imp} v_{imp}^2 k_{ej}, \tag{3}$$

where we use the ejection yield constant k_{ej} for unbonded quartz sand of Greenberg *et al.* (1978).

This model for upper particle size (an ''unprocessed regolith'') is based on consideration of initial fragmentation events for impacts into solid bodies (e.g., Lissauer and Safronov (1991)) and neglects the likely evolution of the regolith size distribution. Ejecta sizes from an evolved regolith should be smaller due to the fact that sustained meteoroid bombardment only decreases regolith particle sizes. We use as an alternate model (a ''processed regolith'') the upper size cutoff,

$$r_{max} \equiv f \cdot r_{impactor}; \qquad f = 0.1 \, .. \, 10, \tag{4}$$

with the same power law distribution. For shallow size distributions, this size cutoff is significantly smaller than that of the unprocessed model: for $q_{ej} = 2.5$, a 100-μm impactor, and the low extreme of Eq. (4), we calculate $r_{max} = 2800$ and 10 μm for the unprocessed and processed models, respectively. For $q_{ej} = 5.5$, the corresponding values are $r_{max} = 48$ and 10 μm.

In both models, the lower end of the size distribution is set at $r_{min} = 0.03$ μm. Such small particles are inefficient scatterers and our results are not strongly sensitive to the lower cutoff size.

Our description of dust production due to meteoroid impacts is not entirely self-consistent because the production model does not depend on regolith history. Dust pro-

TABLE II
G Ring Evolutionary Model Parameter Space

Parameter	Range	Description
q_{ej}	2.5–7.0	Incremental power law size index of regolith ejecta

$m_{largest}$	Unprocessed:
	  $N > m_{largest} \equiv 1$
	Processed:
	  $m_{largest} = 0.1 - 10 \; m_{impactor}$
		Upper size cutoff of regolith ejecta

Flux model	High	Model of Colwell and Esposito (1990); factor of 10^2 higher than their Low model
Surface yield	High (unbonded quartz sand)	Model of Greenberg *et al.* (1978); factor of 13 higher than their Low (bonded quartz sand) model
t_{drag}	10–100 years	G ring plasma drag crossing time, 1 μm particle
f_1	0.12	Mass fraction of largest body at initial G ring disruption event
Parent belt radial width	1000 km	Width of parent body belt
Parent belt cross section	40 km^2	Total parent body cross section
r_{trans}	3–200 μm	Transition particle size from Mie to isotropic scattering model

Note. See Canup and Esposito (1997) for complete description of their model and parameters.

duction and loss due to sweep-up by parent bodies of free particles and subsequent release by mutual parent body collisions is handled self-consistently.

Dust Loss Processes

A ring particle can be considered to be in a Keplerian orbit slightly modified by various drag forces. The main loss process is plasma drag due to direct and distant collisions with corotating particles in the saturnian magnetosphere. Poynting–Robertson drag can be calculated to be roughly two orders of magnitude slower than plasma drag (Burns *et al.* 1979), and we ignore it. We also ignore the effects of radiation pressure, shown by Burns *et al.* (1984) to pump micrometer-particles to a maximum eccentricity $\varepsilon \sim 0.1$, equivalent to roughly the radial width of the G ring and thus not an important loss process.

SC93 calculated that the particle density of the G ring is high enough such that Debye shielding prevents particles from charging significantly; i.e., the Debye length exceeds the average interparticle distance. Because charges on typical particles are small or zero, SC93 found that the Lorentz force is unimportant in the G ring. Although the size distributions we use in this work have interparticle spacings up to two orders of magnitude higher than those of SC93, the particles are still in the Debye shielded regime, and therefore we do not consider the effects of the Lorentz force.

The corotating plasma at the G ring sweeps past Keplerian particles at $v_{rel} \sim 15$ km s^{-1}, transferring angular momentum to them and sweeping them outward from the ring. The time for a dust particle of mass m to migrate from the inner to the outer ring edge is

$$t_{cross} = \frac{F_D}{m \, \Delta v_k}, \qquad (5)$$

where F_D is the total drag force on the particle and Δv_k is the difference in Keplerian velocities at the inner and outer edges of the ring. The total drag force F_D is the sum of drag forces F_{direct} from collisions between ions and dust particles, and $F_{distant}$ from distant "Coulomb collisions." We use the plasma parameters of Richardson (1995) and Bridge *et al.* (1982) modeled from the Voyager encounters: $n_{ion} = 100 \pm 50$ cm^{-3}; $E_{ion} = 10$ eV; $m_{ion} = 16$ amu. Using Eq. (41) of Grün *et al.* (1984) and Eq. (9) of Northrop and Birmingham (1990) we calculate the ratio

$$\xi(1 \; \mu m) \equiv F_{distant}/F_{direct} \sim 2 \qquad (6)$$

and the ring crossing time

$$t_{cross}(r) = \frac{r}{1 \; \mu m} \, 10 \pm 5 \text{ years.} \qquad (7)$$
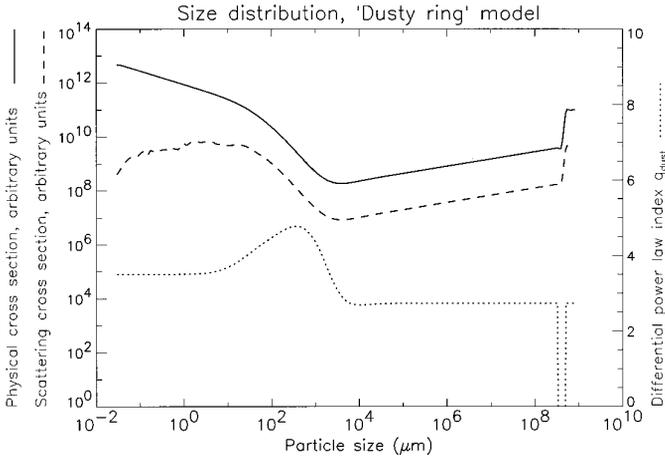
FIG. 1. Typical G ring particle size distribution from Canup and Esposito (1997) model. The top curve is the incremental cross section per size bin, and the bottom curve the power law size index calculated between adjacent bins. The smallest particles ($r \lesssim 10~\mu m$) have a slope $q_{dust} = q_{ej} - 1$, and the slope of the largest bodies ($r \gtrsim 1$ cm) is determined by the initial fragmentation event. The parent body lower size cutoff, $r \sim 0.5$ km, is determined by three-body accretion criteria in the Roche zone. The middle curve is the incremental scattering cross section, i.e., the physical cross section multiplied by the scattering efficiency and phase function at $\theta = 175°$, averaged over wavelength. The smallest particles dominate in the physical cross section but scatter inefficiently; thus, in this case, scattering is dominated by particles in the 1- to 10-μm range, even though the physical cross section is dominated by sub-micrometer particles.

The effect of distant collisions in the G ring has been miscalculated in the past. Northrop and Birmingham (1990) point out that the equations for distant collisions used by Grün *et al.* (1984)—and subsequently Burns *et al.* (1984) and SC93—assume a 1-D, not 3-D, Maxwellian distribution and significantly overestimate the effect of distant collisions. This causes the value of ξ we calculate to be somewhat lower than the $\xi = 100$ calculated by Grün *et al.* (1984). Using $\xi = 2$, we use Eq. (19) of Morfill *et al.* (1983) to confirm a short ring crossing time. We are unable to reproduce the upper end of the $t_{cross}(1~\mu m) = 8$–800 year crossing time calculated by SC93 based on Burns *et al.* (1984); the error in calculating ξ is in the opposite direction to explain this result.

All of the drag times we consider are defined as ring-crossing times for $\Delta a = 7000$ km. Note that the drag times used in the CE97 paper are defined as the time to cross only the central 1000 km.

The steady-state size distributions of CE97 are multi-component power-law distributions (Fig. 1, top curve). The size distribution of the smallest ice particles ($r \lesssim 10~\mu m$) is shallowed by plasma drag and is well-described by the power-law exponent (Burns *et al.* 1984),

$$q_{dust} = q_{ej} - 1. \tag{8}$$

For larger r, q_{dust} steepens (Fig. 1, bottom curve) from this value due to (i) direct grain destruction by meteoroid impact and (ii) dust sweep-up by parent bodies. In dust size regimes where the latter is the dominant loss process,

$$q_{dust} = q_{ej}. \tag{9}$$

Due to the competing effect of direct grain destruction, however, the region where Eq. (9) applies is typically quite narrow. For larger particles, q is determined not by ongoing processes but by the energy of the initial fragmentation event.

IV. LIGHT SCATTERING MODEL

In somewhat the same way that the Earth's blue skies and red sunsets are caused by light scattering by small particles, the color of light scattered by particles in dusty rings is indicative less of their intrinsic color than the particle size. In this paper, we use both the color and angular-dependence of the observations to constrain the size distribution in the G ring.

For sunlight scattered by the rings, the observable quantity is the ring intensity I, normalized by solar flux F at Saturn as (e.g., Showalter *et al.* 1987)

$$\frac{I}{F}(\theta, \lambda) = \frac{\tau \tilde{\omega}_0(\lambda) P(\theta, \lambda)}{4\,\mu}, \tag{10}$$

where τ is the normal optical depth, $\tilde{\omega}_0(\lambda)$ is the single scattering albedo, $P(\theta, \lambda)$ is the normalized scattering phase function for the size distribution, $\mu \equiv \sin(\beta)$, and β is the tilt of the ring plane from edge-on as seen from Earth. For a rectangular G ring cross section with ring width Δa and vertical height Δz, the edge-on optical depth is

$$\tau_{edge} = \tau_{normal} \frac{\Delta a}{\Delta z} \sim 10^{-6} \cdot \frac{7000~\text{km}}{100~\text{km}} \sim 10^{-4}, \tag{11}$$

which is sufficiently low for single scattering to be an accurate approximation.

We define the radially integrated equivalent width

$$\text{EW}(\lambda) \equiv \int_a \frac{I}{F}(\theta, a, \lambda)\, da, \tag{12}$$

which, assuming a radially homogeneous ring, can be written as

$$\text{EW}(\lambda) = \frac{1}{4\,\mu} \int_r Q_{sca}(r, \lambda) P(\theta, r, \lambda) n(r) \pi r^2 \frac{\Delta a}{A}\, dr, \tag{13}$$

where $A = 2\pi a\, \Delta a$ is the area of the ring. Given $n(r)$,

finding the equivalent width reduces to finding functions $Q_{sca}(x)$ and $P(x)$, where we define the size parameter

$$x \equiv 2\pi r/\lambda \qquad (14)$$

and scattering efficiency

$$Q_{sca}(x) \equiv \frac{A_{sca}}{A_{geom}}, \qquad (15)$$

where A_{sca} and A_{geom} are the cross-sectional area for scattering light and the geometric cross-section of the particle. The phase function $P(\theta)$ gives the relative intensity of light as a function of scattering angle θ from the incident beam, normalized such that

$$\int_0^{\pi} P(\theta) \sin \theta \, d\theta = 2. \qquad (16)$$

Functions P and Q_{sca} are dependent on the size, shape, and other physical properties of the scatters. We consider the behavior of P and Q_{sca} in three size regimes corresponding to small, medium, and large particles, and the transitions between these regimes. The regime boundaries are determined by the physical properties of the particles, as described below.

Small Particle Scattering Model

Mie theory (e.g., van de Hulst 1957) gives the scattering properties of spherical, homogeneous particles of arbitrary size x and complex index of refraction $n = n_r + n_i i$, where n_r is the real index of refraction and n_i is the imaginary, absorptive component. From x and n, Mie theory calculates the phase function $P(\theta)$ and the scattering coefficient Q_{sca}. In the very small particle limit ($x \lesssim 1$), Mie scattering reproduces roughly isotropic Rayleigh scattering; for large particles ($x \gtrsim 100$), Mie scattering approaches the geometric optics ("ray tracing") limit, dominated by forward scatter.

The RPX observations of the G ring are within 5° of backscatter. Laboratory and theoretical work near backscatter has identified several effects that are not present at higher scattering angles, including mutual shadowing (e.g., Buratti and Veverka 1983), coherent backscatter (e.g., Mishchenko and Dlugach 1992, Muinonen 1994) caused by phase interference between equal-length paths, and "glory" (e.g., Khare and Nussenzveig 1977) due to resonant waves in spherical particles. The effect of each of these is to increase $P(\theta)$ near backscatter. Mutual shadowing between particles is important only in an optically thick medium, while coherent backscatter from ring particles has only been seen extremely close to backscatter

($\theta \gtrsim 179°$, Mishchenko and Dlugach 1992), and we do not treat it further.

The glory, however, can cause a strong backscatter peak and is likely to be present at the sizes of particles in the rings. The glory is most evident as a narrow peak for $x \gtrsim 200$ and $n \gtrsim \sqrt{2}$. A smaller, wider peak appears near backscatter for somewhat smaller particles, $x \sim 10$–100. Both peaks depend strongly on particle shape and index of refraction. Studies of the glory have indicated that it may be gone or substantially reduced for nonspherical or rough particles (Khare and Nussenzveig 1977), and we therefore look for an appropriate method to treat nonspherical particles in backscatter.

Pollack and Cuzzi (1980) developed a widely used semiempirical model for the phase function of nonspherical particles, based on simple physical principles and parameterization of laboratory scattering results. For small particles ($x \lesssim 5$) they used Mie theory, while for larger particles ($x \sim 5$–20), they constructed phase functions of components from transmitted, diffracted, and surface-reflected light. Laboratory work allowed them to parameterize the shape and relative contribution of each component; because their study focused on aerosols, they did not consider particles larger than $x \sim 20$. Laboratory experiments that they considered (e.g., Zerull and Geise 1974, Holland and Gagne 1970) showed monotonically *decreasing* $P(\theta)$ toward backscatter, and their model thus included no backscatter peak. However, the particular experiments used did not measure any closer to backscatter than $\theta \sim 170°$, and the model's linear extrapolation to larger angles may have missed any very real backscatter peak.

Liou *et al.* (1983) used a combination of ray tracing and Fraunhofer diffraction to calculate the phase function for large ($x \sim 1000$) cubes and bricks. They observed a very strong, wide backscatter peak from rays undergoing between three and five internal reflections. Much of this backscatter is likely to be due to the trough and corner retroflections of the exact particles used and is likely to be significantly reduced for rough particles (e.g., Muinonen *et al.* 1989, 1996).

In their analysis of the Saturn F ring, Showalter *et al.* (1992) used the results of Liou *et al.* (1983) to add a backscatter peak to the Pollack and Cuzzi (1980) model. Because of uncertainties of the applicability of (i) the Liou *et al.* results to nonrectangular particles and (ii) their combining of different parts of phase functions for measurements of $x \sim 10$ and $x \sim 1000$ particles, we have not used the Showalter *et al.* (1992) modification of the PC80 model.

The transition-matrix ("T-matrix") method developed by Waterman (1971) is a series solution to Maxwell's equations that is similar to Mie theory, but that can be applied to nonspherical particles. Theoretically, the T-matrix method can be applied to particles of arbitrary shape and size; however, considerable analytic effort is required for new

shapes (Draine 1988), and computation time increases quickly with size (x^3). Although the method is not new, its use has become practical only recently due to computational and analytical advances. Mishchenko *et al.* (1996, 1997) have recently used it to calculate scattering from ensembles of randomly oriented spheroids, cylinders, and Chebyshev particles. Current calculations are limited to $x \lesssim 70$ for axisymmetric particles, and the method is several orders of magnitude slower than Mie scattering for the size ranges computed here. Comparisons of phase functions calculated from prolate and oblate spheroids have been found to match very closely observed phase functions from highly nonuniform particles such as micrometer-sized soil particles. We have found phase functions from T-matrix calculations for ensembles of randomly oriented spheroidal low-n ($\lesssim\sqrt{2}$) particles to be qualitatively similar to that from Mie scattering, with a somewhat wider, weaker backscatter peak.

Although T-matrix computations would be ideal for our work, the current size limitations prevent us from using it. We have therefore used exclusively Mie scattering for our small particles, and preliminary work with T-matrix calculations for small particles suggests that the effect of this choice is that our computed dust optical depths may be high by a factor of up to two. We do not believe that the difference between spherical and nonspherical particles otherwise significantly affects our scattering calculations; however, computations for large nonspherical particles would be necessary to quantify the difference completely.

We have taken the index of refraction to be that of slightly contaminated amorphous ice, $n = 1.27 + 0.001i$ for visible light, measured by Berland *et al.* (1995), slightly lower than that of crystalline ice ($n = 1.33 + 0.001i$) used by SC93. The difference between these two indices has very little effect, however, nor does varying the imaginary index of refraction in the range $n_i = 10^{-3\pm1}$. The $n_i = 0.001$ assumed corresponds to an exponential absorption depth of $r \sim 20$ μm in the visible. A compilation by Warren (1984) indicates that these optical properties are nearly constant across the visible and at our far wavelength range, $\lambda = 2.26$ μm.

Large Particle Scattering Model

As with previous studies of ring light scattering (e.g., Showalter *et al.* 1992, Estrada and Cuzzi 1996), we assume that the macroscopic particles of the rings have spectra similar to that of contaminated water ice. We use the spectrum $\tilde{\omega}_0(\lambda)$ of Saturn's main rings from Clark *et al.* (1980) normalized to a *V*-band albedo of 0.7 (e.g., Esposito *et al.* 1984), typical of relatively fresh, uncontaminated surfaces. This spectrum is slightly red in the visible and drops off in the IR. The phase function $P(\theta)$ observed by Voyager of Europa was determined by Buratti and Veverka (1983)

to be very nearly that of a Lambert sphere; we assume Lambertian scatterers.

For simplicity we do not include the diffraction peak from large particles because the peak is not typically observed; i.e., we assume $Q_{sca} = 1$. Therefore, when we call a particle "backscattering," we refer only to the nondiffracted component.

We note that although the contribution to EW from parent bodies is small, the contribution from other macroscopic particles can be significant. This is a substantial difference between our model and that of SC93.

Intermediate Particle Scattering Model

As Showalter *et al.* (1992) notes, the phase functions for the large and small particle limits are fundamentally different: Mie theory used for small particles shows forward scatter, with their phase functions *decreasing* monotonically with scattering angle, while the Lambert scattering model for large, opaque bodies is dominated by backscatter, with phase functions *increasing* with scattering angle (e.g., Fig. 5b). Previous photometric models (e.g., Showalter *et al.* 1992, Showalter 1996) that included reflectance from both large and small particles have transitioned between these two regimes with a step function placed at a cutoff value between 20 and 100 μm. In the size distributions considered in those studies, there was very little optical depth at the transition size, so the ring reflectance was insensitive to the specific parameters of the transition. However, recent laboratory work suggests that a more detailed scattering model in this region may be necessary.

While clear, spherical, crystalline ice can be treated by Mie theory, studies by McGuire and Hapke (1995) of particles with high internal scattering indicate that Mie theory may not be applicable for such particles. This is consistent with everyday observations: a large clear sphere of ice transmits light by forward scatter and can be described by geometric optics; however, a snowball of the same size is nearly opaque and strongly backscatters. McGuire and Hapke (1995) studied internal scattering by introducing 0.3-μm TiO$_2$ particles into centimeter-sized smooth, clear resin spheres they constructed in the lab. Spheres with varying amounts of internal scattering were fabricated, and the phase function of each measured. The amount of internal scattering was specified by nondimensional parameter sD, with internal scattering coefficient s (cm^{-1}) and particle diameter D. For $sD = 0$, they observed Mie scattering in the geometric optics limit; $sD = 35$ yielded approximately isotropic scattering, and at $sD = 275$ the spheres scattered as Lambert surfaces. These results have been subsequently confirmed by Monte Carlo simulations by Mishchenko and Macke (1997), with the additional result that voids can be treated in the same fashion as the high-n inclusions of McGuire and Hapke.

TABLE III
Scattering Transition Sizes

$r \leq r_{trans}/7$	Mie scattering
$r_{trans}/7 < r < r_{trans}$	Linear combination: Mie and Isotropic phase curve and spectrum
$r_{trans} < r < r_{trans} \cdot 7$	Linear combination: Isotropic and Lambert phase curve and spectrum
$r \geq r_{trans} \cdot 7$	Lambert scattering

Internal scattering such as that observed by McGuire and Hapke (1995) is likely to be present in amorphous ice. A microporous, amorphous form of water ice is formed by slow condensation at temperatures below 120 K; between 120 and 160 K, a denser, optically clear form of amorphous ice is formed, and above 160 K crystalline ice is formed (e.g., Brown *et al.* 1996). Amorphous ice will eventually undergo a one-way transition to crystalline ice: for $T > 160$ K, the transition is nearly immediate, while for $T < 77$ K, the transition time is roughly the age of the Solar System (Schmitt *et al.* 1989). Studies of protosolar nebula formation by Mekler and Podolak (1984) have indicated that present-day small icy bodies formed of uncontaminated H_2O beyond 7.5 AU are likely to have never crystallized and are good candidates for microporous amorphous ice. The crystalline and amorphous phases of ice can be distinguished by spectral features near 3 and 45 μm (e.g., Moore and Hudson 1992); however, no data for the G ring exist at these wavelengths.

Based on the modeling of Mekler and Podolak (1984), we have assumed that the ring particles are made of microporous amorphous water ice, and we assume that the internal voids in this ice can be treated as internal scatterers. We estimate the function $sD(x)$ for ring particles, and use an appropriate phase function for each size regime as McGuire and Hapke (1995) identified.

Experimental studies by Schmidt *et al.* (1987) of amorphous water ice indicate that the transition to isotropic scattering ("the transition size") occurs in the several-micrometer range for visible light. This study used thin vapor-deposited ice films, and observed the backscatter from the films while increasing their depth. Detailed behavior of the transition is still largely uncharacterized; for instance, Schmidt *et al.* (1987) looked only at unprocessed, uncontaminated films of ice, and not the roughly spherical particles present in the rings.

The transition size can also be calculated using the known characteristics of the internal scatterers. Adsorption studies of N_2 into amorphous ice by Mayer and Pletzer (1986) measure an internal scattering area of up to 400 m^2 g^{-1}, and find that most of this surface area is in molecular-sized holes of radius $a \sim 20$ Å. Using the criteria of McGuire and Hapke for isotropic scattering, and treat-

ing the voids as individual Rayleigh scatterers, we calculate that the amorphous ice examined by Mayer and Pletzer should reach isotropic scattering at $r_{trans} \sim 300$ μm; for $a \sim 50$ Å, isotropic scattering is reached at $r_{trans} \sim 5$ μm. Thus, although large uncertainties exist in the laboratory work, two independent methods lead us to believe that internal scattering is important in this size regime.

In addition to internal scattering, scattering from roughened particle surfaces may also be important. Johnson *et al.* (1985) note that several studies (Brown *et al.* 1978, W. D. Smythe 1984 unpublished) of clear, smooth ice surfaces bombarded by fast (0.1–10 MeV) ions rapidly became highly reflecting. Electron microscope examination by Johnson *et al.* (1985) of the sputtered surfaces revealed them to be dominated by micrometer-sized pits, changing the surfaces' forward scattering to highly non-Lambertian backscattering. Johnson *et al.* (1985) have indicated that the particle environment near the G ring is sufficient for sputtering to be an important process; they note that this process could explain, for instance, the non-Lambertian scattering strongly enhanced toward backscatter of Enceladus, which is slightly outside the G ring's orbit at 4 R_s. Further studies by Strazzulla *et al.* (1988) were performed by irradiating 10 K water ice films with 150 keV He$^+$ ions. They observed that the phase function became more iso-
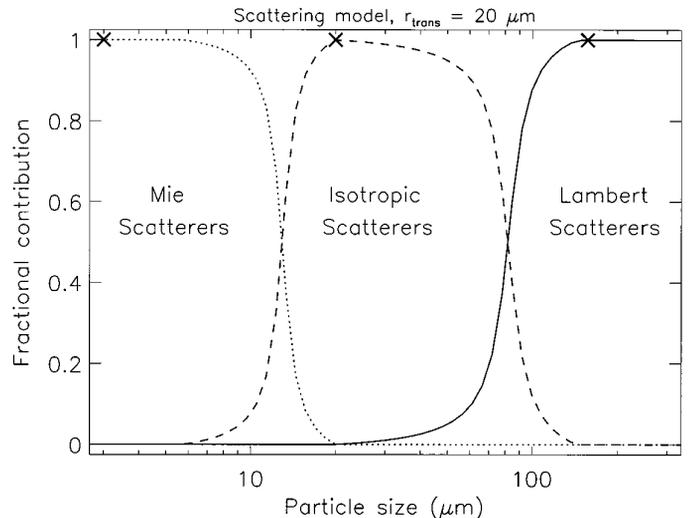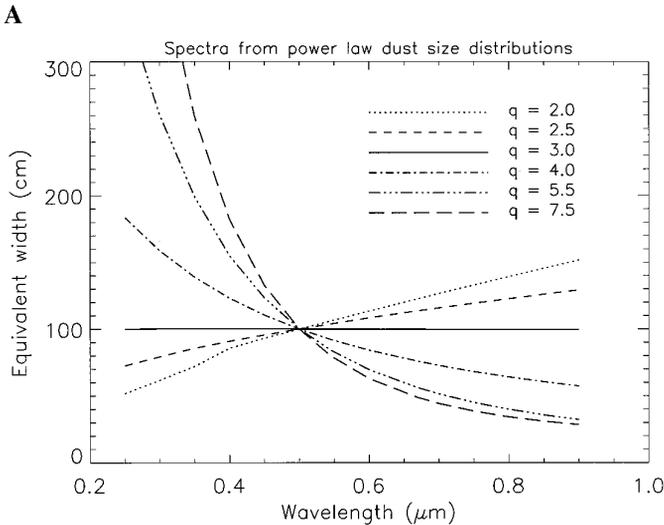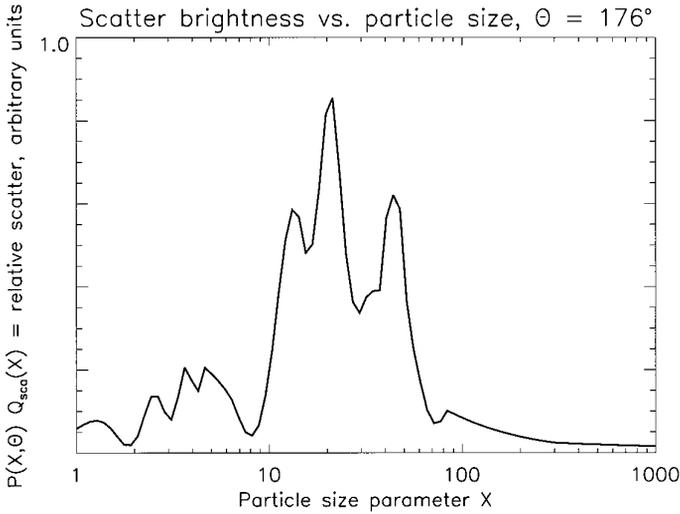

FIG. 2. The transition sizes for our three-component scattering model. The smallest particles are treated as Mie scatterers, intermediate particles as isotropic scatterers, and the largest as Lambert scatterers. The transition sizes, marked with symbols, are as identified by McGuire and Hapke (1995). Particles near region boundaries are treated as a combination of scattering types. Mie theory determines the spectrum of the small particles, while we use the spectrum of Saturn's main rings for intermediate and large particles. The transition between the regimes is caused by internal scattering due to voids in amorphous water ice, as described in the text. This figure assumes an internal scattering coefficient $D = 0.9$ μm^{-1}; this is a parameter that we vary by varying r_{trans} in the range 1–300 μm.

Scatter brightness vs. particle size, $\Theta = 176°$

A

Spectra from power law dust size distributions

B

FIG. 3. (a) In Mie scattering, each wavelength scatters strongly only for a narrow range of particle size; for water ice at $\theta \sim 175°$, this size range is $x \sim 10–50$. Below this range Q_{sca} decreases quickly and above this range, the phase function P is dominated by forward scatter. Individual wavelengths in the scattered spectrum can be directly related to a particular particle size range, and—were the ring to consist only of a power-law size distribution of Mie scatterers—the size distribution slope could be directly related to the ring's color. This figure is calculated for the backscatter angle seen during the ring crossing; however, similar size-selection features are seen over a wide range of scattering angles. For reasonably physical size distributions, width will smear out the detail shown here and the function is single-peaked. (b) The power law slope of a distribution of Mie scatterers is directly related to its reflected color. Distributions dominated in cross section by large particles ($q_{dust} < 3$) scatter long-wavelength light most efficiently and appear red; distributions dominated by small particles ($q_{dust} > 3$) appear blue. All curves are for $r = 0.01–10$ μm, $n = 1.27 + 0.001i$, and are normalized at 0.5 μm.

tropic after irradiation; however, detailed characterization of the phase functions have yet to be made.

We address both internal- and surface-scattering effects by leaving as a parameter r_{trans}, defined as the size at which

particles scatter isotropically. Thus, the phase function is a function of particle size (Table III; Fig. 2), with the transitions between the three scattering regimes chosen to correspond to those measured by McGuire and Hapke (1995). Table III shows how the single parameter r_{trans} subdivides the size distribution and the phase functions used for each size. We vary t_{trans} in the range 1–300 μm. Because the scattering efficiency of internal scatterers is wavelength-dependent, we vary r_{trans} linearly with λ; e.g., we assume the transition size at $\lambda = 1$ μm to be double that at $\lambda = 0.5$ μm. All transition sizes in this paper are given for $\lambda = 0.5$ μm.

The ring brightness at each wavelength is the sum of the Mie, isotropic, and Lambert reflectances. The latter two components have a fixed color and phase function, while that of the Mie component depends on the particle size distribution.

### Spectrum from Small Particles

The intensity scattered at a fixed θ from small particles is proportional to $P(x)Q_{sca}(x)$ (e.g., Eq. (13)). For spherical particles at $\theta \sim 175°$ observed at the RPX events, this product is a peaked function which reaches a maximum in the range $x \sim 10–50$ (Fig. 3a): below this size, the scattering efficiency decreases, and above it, forward scatter dominates the Mie phase function. Light scattered at this angle is dominated by particles in this range; both significantly larger and smaller particles are "invisible" to an observer at backscatter. Thus, in much the same way that kernel functions (e.g., Goody and Yung 1989) may be used to probe atmospheric vertical structure at a particular temperature, each part of the reflectance spectrum probes abundance near a particular particle size.

If q_{dust} is such that the cross section in logarithmically spaced bins of r decreases with r (i.e., $q_{dust} > 3$, and the cross section is dominated by *small* particles), *blue* wavelengths will be most visible in the reflected spectrum (Fig. 3b). If, on the other hand, the bulk of the surface area is in *large* particles (i.e., $q_{dust} < 3$) which are more strongly reflecting and thus seen best at longer wavelengths, the scattered light will appear *reddened*. Thus, the backscattered spectrum from a power law distribution of scatterers can be directly related to the slope of the distribution. This differs from the result of Showalter *et al.* (1991), which showed no strong relation between the two. For generalized (i.e., non-power-law) size distributions, the inverse problem is nonunique: multiple size distributions can be consistent with the same spectrum.

The color of Earth's sky and sunsets is caused by Rayleigh scattering by smaller particles than we consider here (in effect, the monotonic left half of Fig. 3a) and does not correspond in the same way to size distribution.
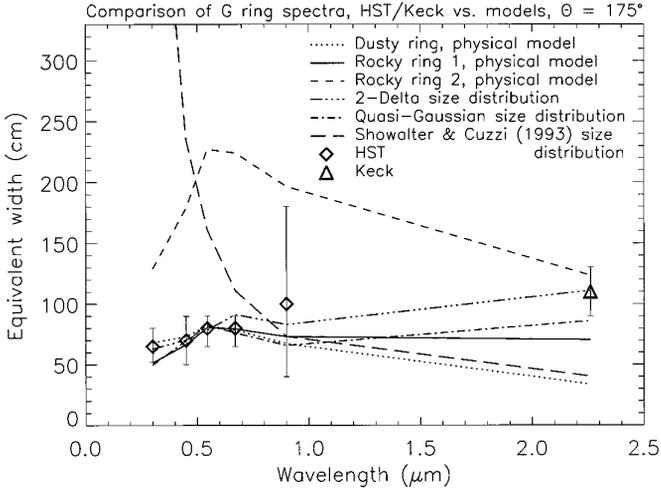
A
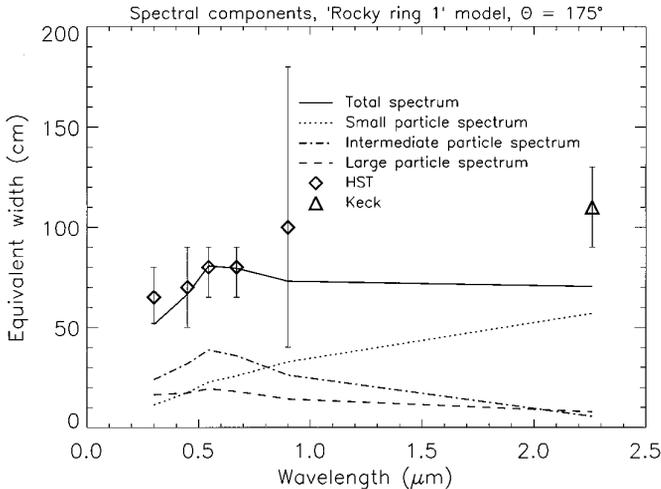
B

FIG. 4. (a) We identify several fits to the HST and Keck spectrum. The size distribution of Showalter and Cuzzi (1993) is too blue to fit the spectrum. Other models fit the visible spectrum well, although some underestimate IR brightness. HST data are by Nicholson *et al.* 1996; Keck observation is by de Pater *et al.* (1996). (b) Each spectrum is the sum of components from small, intermediate, and large particles. Although the large-particle spectrum is dark in the IR, Mie scattering from small particles is still efficient at the wavelength. Therefore, an IR-bright ring implies the abundance of small particles.

V. MODEL RESULTS

We have made a grid of models, which vary the model parameters q_{ej}, m_1, t_{drag}, and r_{trans} across their estimated ranges, as indicated in Table II. For each of the $N \sim 800$ models, we have qualitatively assessed the goodness-of-fit to (i) the spectrum from HST and Keck, (ii) the phase curve from Voyager and HST, and (iii) the m_{rms} derived from the plasma instruments. We find that q_{ej} in the range 2.5–4.5, with appropriate selection of the other parameters,

can produce models that are reasonably consistent with the observations (Figs. 4, 5). Characteristic fits from the physical models are summarized in Table IVa.

For the low q_{ej} solutions (e.g., $q_{ej} = 2.5$, "Rocky ring 1") the spectrum and phase curve match the observations well. This model, and several others, overestimates m_{rms} by a factor of up to 30; we discuss possible explanations for this difference below.

The "unprocessed regolith" model is inconsistent with a low q_{ej} because this regolith model implies a large maximum ejecta particle size. The total cross section of these large particles is thus significant; because large Lambert scatterers are observed to be dark in the IR, the spectrum
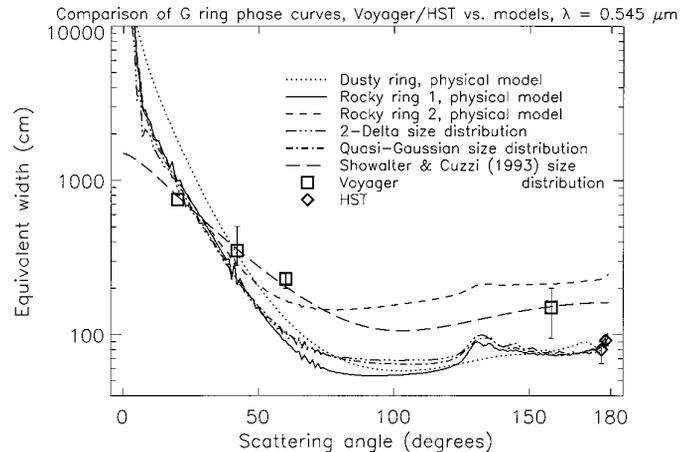
A
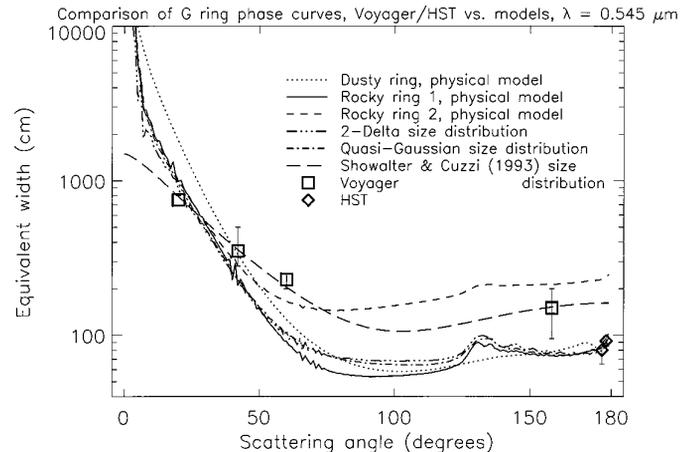
B

FIG. 5. (a) Corresponding fits to the Voyager and HST phase curve. The decrease near backscatter ($\theta = 175°$) is not reproduced by standard scattering methods and may be an observational effect or an indication of a change in the ring. Voyager data are by Showalter and Cuzzi (1993); HST data are by Nicholson *et al.* (1996) and French *et al.* (1997). (b) The total phase curve from a size distribution is the sum of components from the three scattering types. The phase curve for Mie (forward-scattering) and Lambert (backscattering) particles are in opposite senses.

TABLE IV
Best Fits to Observations

Name	q_{ej}	$m_{largest}$	t_{drag} (1 μm)	r_{trans} (μm)	m_{rms} (model)/ m_{rms} (Voyager)[a]
		a. Selected evolutionary models			
Rocky ring 1	2.5	0.1 $m_{impactor}$	500 Years	60	27
Rocky ring 2	2.5	0.1 $m_{impactor}$	700 Years	20	27
Dusty ring	4.5	0.1 $m_{impactor}$	500 Years	3	28
		b. Nonevolutionary models			
		Size distribution		r_{trans} (μm)	
quasi-Gaussian		$r_0 = 13$ μm, $\sigma = 0.5$		15	0.9
δ-function ring		$r = 8.2$ μm, 21 μm, 100 m		15	2.3
Showalter and Cuzzi 1993		$q_{dust} = 6.0$		—	0

[a] Considers only mass above detector threshold; see text.

of this ring model is too IR-dark to match the observations. However, smaller Mie scatterers do reflect efficiently at this wavelength. Therefore, an IR-bright ring implies a cross section dominated by small particles, such as that from the "processed regolith" model, rather than large particles, such as that from the "unprocessed regolith" model.

A second solution for low q_{ej} ("Rocky ring 2") fits the Voyager phase curve well, but overestimates the visible spectrum. The size distributions of the two "Rocky ring" models are similar; the primary difference is the value of r_{trans}, taken to be 60 and 20 μm in the two models, respectively. In the latter model, the smaller transition size means that more small particles are treated as isotropic, rather than Mie, scatterers. The phase curve fits particularly well because the nearly isotropic phase curve from Voyager can be matched well by a population of intermediate-sized isotropic scatterers of $r \sim r_{trans} \sim 20$ μm from our three-component scattering model. In contrast, the scattering model of SC93 included only one type of isotropic scatterer: very small particles in the Rayleigh regime.

In the case of high q_{ej} (e.g., $q_{ej} = 4.5$, "Dusty ring" model), the strong blue scattering from small particles of $r_{trans} < 3$ μm is partly canceled by the intrinsic red color of the larger particles. This model fits the phase and m_{rms} observations well, but slightly underestimates the IR brightness. Models with $q_{ej} \gtrsim 5$ are too blue to match the HST spectrum; this confirms the initial finding of Nicholson *et al.* (1996) that the size distribution of SC93 is inconsistent with that implied by the broadly red HST spectrum.

The $q_{dust} = 6$ size distribution identified by SC93 fits the phase curve extremely well, but is too strongly blue to match the observed spectrum, even for r_{trans} as low as 0.5 μm. This steep size distribution also predicts no detectable PWS/PRA events. Therefore, we do not consider the SC93 distribution to be consistent with the bulk of the observa-

tional data. Although the three solutions shown use the "processed regolith" model, the "unprocessed regolith" model is consistent in some of the high-q_{ej} cases not shown. The difference between the two models is their upper size cutoff; for $q_{ej} > 3$, the optical depth is dominated by small particles and the upper ejecta size cutoff is relatively unimportant.

In addition to size distributions that result from the CE97 evolutionary model, we have identified two "ad hoc" size distributions that fit the observational data (Table IVb). The first of these is the quasi-Gaussian of the form specified by Hansen and Travis (1974),

$$n(r) = Cr^{(1/\sigma^2-3)}e^{-(r/r_0\sigma^2)}, \tag{17}$$

with characteristic size $r_0 = 13$ μm and fractional dispersion $\sigma = 0.5$. For this size distribution the visible spectrum and forward scatter components are due primarily to small particles, and the IR and backscatter reflectance are primarily from medium-sized particles.

We also find a multi-component delta-function distribution, with particles at 8 and 21 μm and 100-m parent bodies. This distribution provides an excellent fit to spectral, phase, m_{rms}, and proton absorption observations. However, it is not clear what physical processes could create or sustain such a ring. This distribution approximately straddles the quasi-Gaussian distribution above; other similar distributions centered near $r \sim 15$ μm also fit the observations.

These ad hoc distributions are examples of the non-uniqueness of the inversion process. Superpositions of different models are possible; for instance, the quasi-Gaussian distribution may be added to the dusty ring model and fit the observations. Using a physical model significantly constrains the possible solution space; however, it is possible that fits to the observational data exist that we have not considered. We stress, however, that our power-law and ad hoc size distributions fit the observed data regardless of assumptions made in the physical model.

VI. DISCUSSION

We have found several models that fit the observations well. In this section, we describe the differences between our solutions and the data and various uncertainties in our model.

Because the Keck data were taken only during the Earth RPX events, the ring appeared edge-on and it was necessary to assume a radial profile in order to calculate the radially integrated EW. M. R. Showalter (pers. commun. 1996) indicates that the G ring radial profile of SC93 was assumed in this analysis. Recent observations of the radial profile by French *et al.* (1997) have confirmed SC93's result and thus this portion of the Keck data reduction. Some of the HST data were taken during the Sun RPX event when

the ring plane did not appear edge-on and thus do not depend on a radial profile model.

Variations in calibration and processing between the Keck and HST observations may cause additional uncertainties in comparing their absolute values. J. M. Bauer (pers. commun. 1996) indicates that their August 1996 2.2-μm IRTF observations confirm the radially integrated equivalent width of de Pater *et al.* (1996); Bauer *et al.* (1997) present IRTF results only in terms of vertically integrated equivalent width.

The individual nontargeted images used for the phase curve presented in SC93 were subject to substantial background subtraction and frame coaddition; without processing, the G ring is visible in only 2 of the 13 frames that SC93 identify. Although statistical error bars are presented in SC93, we must use care when interpreting these data given the extreme conditions under which they were obtained. The HST data were obtained, reduced, and calibrated under consistent and well-characterized conditions; for this reason, when necessary we have chosen to optimize fits to the spectrum rather than the phase curve.

The m_{rms} from many of our models is up to a factor of 30 higher than that computed by Tsintikidis *et al.* (1994) based on reanalysis of the Voyager PWS/PRA data. Several factors must be considered when comparing the two results. The error in measuring the mass of a single particle comes from at least two sources: (i) uncertainty in the impact ionization yield, unknown to a factor of 10 (Tsintikidis *et al.* 1994), and (ii) instrumental uncertainties such as antenna potential and spacecraft capacitance. Furthermore, sampling statistics also must be considered due to the low optical depth and number of particle–spacecraft collisions in a typical passage through the ring. Using a Monte Carlo method, we have simulated normal spacecraft trajectories through the ring using a detector with $m_{min} = 5.4 \times 10^{-9}$ g threshold estimated for the PWS/PRA instruments, and found that the observed 1σ m_{rms} for individual runs varied by up to a factor ~10. Therefore, based on the uncertainties in comparing the Voyager and model results, we have computed average values for m_{rms} based on a large number of passages through the ring, but have not used m_{rms} as a strong constraint to our models. Furthermore, recent modeling of PWS/PRA data by Meyer-Vernet *et al.* (1997) indicates that the *in situ* observations are caused by much smaller particles ($r \sim$ few μm) than indicated by Tsintikidis *et al.* (1994) and of comparable size to those that our photometric modeling indicates.

As discussed earlier, the effect of nonspherical particles may be detectable near backscatter, and may decrease the reflectance by up to a factor of 2 for wavelengths at which the reflectance is from small particles. In most of our solutions, the visible reflectance is due to medium-sized particles, and the IR reflectance due to small particles. Thus, we would expect non-spherical particles to make the ring darker by up to a factor of 2 in IR and somewhat less changed in the visible. This effect is within the uncertainties of the observations and our particle size distributions.

As indicated by Hamilton and Burns (1994), Saturn's E ring may provide an additional source of particles for the G ring. They showed that precession resonances can pump 1-μm particles in the E ring to high eccentricity, where they cross the F and G rings and are ultimately absorbed by the A ring at 2.2 R_S. These particles cross the G ring and we briefly consider their effect as an impactor source into G ring parent bodies.

The E ring number density is observed to fall off inward of its peak at 3.8 R_S as a^{15} (Showalter *et al.* 1991). Assuming that the entire optical depth is due to 1-μm particles, calculating a relative impact velocity $v_{impE-G} = 5.5$ km s^{-1}, and using the mass yields for impacts into unbounded quartz sand of Greenberg *et al.* (1978), we find the total mass yield from E ring particles onto G ring parent bodies:

$$\dot{M}_{Ering} = n_{imp}k_{ej}\tfrac{1}{2}m_{imp}v_{impE-G}^2 \simeq 4 \text{ g s}^{-1}. \quad (18)$$

Using the Colwell and Esposito (1990) "high flux" meteoroid model used in CE97, we calculate the mass yield from meteoroid impacts onto parent bodies:

$$\dot{M}_{meteoroid} \simeq 3 \text{ g s}^{-1}. \quad (19)$$

Thus, although the mass flux of E ring particles significantly exceeds that of meteoroids, the E ring particles impact into parent bodies at a much lower velocity, and the total yields from each source are surprisingly comparable.

The effect of E ring particles is not incorporated into the CE97 model, and we have not considered this issue further. Better modeling of E ring physical processes, such as particle size distributions produced from the Enceladus surface, is necessary before the effects of its particles on the G can be considered; for instance, the model developed by Hamilton and Burns (1994) generates many more small particles than the photometry by Showalter *et al.* (1991) indicates. Transport between the rings may have interesting consequences: for instance, could the $r = 1$ μm flux from the E ring contribute to an $r = 15$ μm quasi-Gaussian distribution in the G ring?

The solutions presented here are tuned to produce and maintain the maximum ring optical depth; i.e., most of our parameters are set to their extremes to maximize particle production and minimize particle loss. Indeed, it is a bit of a surprise that the ring *is* so bright. At least two explanations are possible. The first is that we have underestimated dust sources or overestimated dust loss. We have addressed this issue by increasing the particle lifetime against plasma drag to longer times than indicated by the Voyager plasma

observations. A similar approach would be to increase the cross section of parent bodies; doubling the cross section has roughly the same effect as doubling the drag lifetime. Other factors may be important too; for instance, the effect of crossing E ring particles has not been included.

It is surprising that the drag times required by our model are so much longer (by two orders of magnitude) than those indicated by (7). We do not have a good explanation for this result. We note that the main loss process for micrometer-sized particles at the outer edge is particle sputtering, which is estimated by SC93 to be 10^4 years for $r = 1$ μm particles. Our modeling is inconsistent with such a long sputtering time; rather, the nearly radially symmetric ring profile suggests that the drag and sputtering lifetimes would be comparable.

A second explanation for the apparent difficulty in maintaining a bright ring is that our assumption of a near-steady-state ring may be incorrect. This may relate to an unusual feature of the composite Voyager and HST phase curve: the V-band HST observation may suggest a local *decrease* in brightness toward backscatter, while results from particle scattering models nearly always indicate a local *increase* toward backscatter. This result is somewhat unexpected and—if it is a real effect—could be indicative of a limitation of our optical model or an actual change in the ring between the Voyager and HST observations. In the latter case, it is possible that (i) the ring is azimuthally non-uniform and/or (ii) the ring is time-variable. The first situation is inconsistent with imaging results, which have not suggested any asymmetry. The second case is possible, as variations in the ring's brightness would be expected after every impact event. In the CE97 models, mutual parent body collisions necessary to approximately double the optical depth occur with frequency

$$t_{\text{collision}} \sim \frac{1}{\Omega \tau_{\text{parent}} n_{\text{parent}}^2} \sim 10^{2-3} \text{ years} \qquad (20)$$

for parent body optical depth $\tau_{\text{parent}} \sim 10^{-8}$, number of parent bodies $n_{\text{parent}} \sim 5\text{--}15$, and Keplerian orbital speed Ω.

The relaxation time after such a perturbation is model-dependent based on the dominant dust size and thus dominant loss process: for a ring dominated by micrometer-sized particles, plasma drag is the dominant loss process and

$$t_{\text{relax}}(1 \text{ }\mu\text{m}) \sim t_{\text{drag}}(1 \text{ }\mu\text{m}) \sim 10 \text{ years}. \qquad (21)$$

For a ring dominated by large particles where parent body sweep-up is the dominant loss process,

$$t_{\text{relax}}(1000 \text{ }\mu\text{m}) \sim \frac{1}{\Omega \tau_{\text{parent}}} \sim 10^4 \text{ years}. \qquad (22)$$

Thus, it is possible, if statistically unlikely, that the difference between Voyager and HST optical depths in backscatter could be explained by collisional release of small dust particles just prior to the Voyager encounters.

Although several of our parameters—for instance, the particular details of the scattering transition sizes and the ejection model—have high uncertainty, the specific results of our models are relatively insensitive to such details, in the sense that the effects of modifying one parameter can generally be compensated for by changing other parameters. Therefore, we have not attempted to unrealistically constrain unknown parameter values.

VII. CONCLUSIONS

Using a physical, evolutionary model of planetary ring evolution, coupled with a detailed particle scattering model, we have determined a range of size distributions for the Saturn G ring which provide a good fit to the complete set of spacecraft and Earth-based observations. This range is characterized by a differential power law size distribution of exponent $q_{\text{dust}} = 1.5\text{--}3.5$.

We find that the size distribution indicated by the SC93 analysis of Voyager photometry, $q_{\text{dust}} = 6 \pm 1$, is not supported by the observations. Our more detailed light scattering model is able to explain the nearly isotropic phase curve presented in SC93 using a size distribution of significantly larger particles; experimental work by McGuire and Hapke (1995) indicates that isotropic scattering is caused both by small Rayleigh scatterers and by much larger internally scattering particles.

Several ad hoc size distributions also fit the observations; the most physically plausible is a quasi-Gaussian distribution of particles at $r \sim 13$ μm. The inversion process is nonunique and it is possible there are additional distributions we have not identified.

We have used data from an array of observations: HST and Keck visible and IR spectra, Voyager photometry and phase curves, Voyager dust impact detections, and Pioneer particle absorption signatures. The CE97 physical model we use tracks the size distribution of a debris swarm from its initial formation following a satellite disruption into a steady-state ring. Our particle scattering model considers several optical phenomena that have not been considered in depth in previous studies of light scattering from planetary rings: namely, the behavior of backscatter peaks caused by realistic non-spherical particles and the effects of internal and surface scattering on particle phase functions. The scattering model includes contributions from Mie scatterers, isotropic scatterers, and Lambert scatterers, as well as intermediate particles which are a combination of these three scattering types.

This study forms the first complete analysis of the G ring RPX data, and the first analysis of that ring's spectrum.

VIII. FUTURE WORK

Observations from the Cassini spacecraft will include IR–UV spectral and phase coverage of the G and other dusty rings. The wider wavelength range of the Cassini instruments may allow observation of scattering from larger particles (in IR) and smaller particles (in UV) than the current observations allow; however, water absorption bands cause the reflectivity of ring particles to drop significantly outside of the wavelength range considered in this paper. Phase coverage of the ring will be important; although our modeling indicates that phase functions are less strongly dependent on particle size distribution than are spectra, the combination of phase information and spectra together is significantly more useful than either one alone. Important measurements will also include *in situ* dust particle detection in the region surrounding the ring, constraint of the parent body cross section and radial and vertical extent from its effect on the charged particle spatial distribution, and constraint on the meteoroid flux at Saturn.

We use only relatively simple regolith models in this work, while size selection effects and regolith processing history may cause more complex distributions to be more accurate. We note that the non-power-law nature of the meteoritic flux (e.g., Grün *et al.* 1985), grain size effects (e.g., Kendall 1978), and mutual particle grinding (e.g., Austin *et al.* 1986) may all be important in determining the size regolith distribution. More detailed theoretical and laboratory modeling of the regolith evolution process is an open area for future work, in particular because the smallest particles in the rings are both the most visible and thus the most indicative of ring composition, size distribution, and processing history.

REFERENCES

Aubier, M. G., N. Meyer-Vernet, and B. M. Pederson 1983. Shot noise from grains and particle impacts in Saturn's ring place. *Geophys. Res. Lett.* **10,** 5–8.

Austin, L. G., C. A. Barahona, N. P. Weymont, and K. Suryanarayanan 1986. An improved simulation model for semi-autogenous grinding. *Powder Technol.* **47,** 265–268.

Bauer, J., J. J. Lissauer, and M. Simon 1997. Edge-on observations of Saturn's E and G rings in the near-IR. *Icarus* **125,** 440–445.

Berland, B. S., D. E. Brown, M. A. Tolbert, and S. M. George 1995. Refractive index and density of vapor-deposited ice. *Geophys. Rev. Lett.* **22,** 3493–3496.

Bridge, H. S., and 14 colleagues 1982. Plasma observations near Saturn—Initial results from Voyager 2. *Science* **215,** 563–570.

Brown, D. E., S. M. George, C. Huang, E. K. L. Wong, K. B. Rider, R. S. Smith, and B. D. Kay 1996. H_2O condensation coefficient and refractive index for vapor-deposited ice from molecular beam and optical interference measurements. *J. Phys. Chem.* **100,** 4988–4995.

Brown, W. L., L. J. Lanzerotti, J. M. Poate, and W. M. Augustyniak 1978. "Sputtering" of ice by MeV light ions. *Phys. Rev. Lett.* **40,** 1027–1030.

Buratti, B., and J. Veverka 1983. Voyager photometry of Europa. *Icarus* **55,** 93–110.

Burns, J. A., P. L. Lamy, and S. Soter 1979. Radiation forces on small particles in the Solar System. *Icarus* **40,** 1–48.

Burns, J. A., M. R. Showalter, and G. E. Morfill 1984. The ethereal rings of Jupiter and Saturn. In *Planetary Rings* (R. Greenberg and A. Brahic, Eds.), pp. 200–272. Univ. of Arizona Press, Tucson.

Canup, R. M., and L. W. Esposito 1995. Accretion in the Roche zone: Coexistence of rings and ringmoons. *Icarus* **113,** 331–352.

Canup, R. M., and L. W. Esposito 1997. Evolution of the G ring and the population of macroscopic ring particles. *Icarus* **126,** 28–41.

Clark, R. N. 1980. Ganymede, Europa, Callisto, and Saturn's rings: Compositional analysis from reflectance spectroscopy. *Icarus* **44,** 388–409.

Colwell, J. E., and L. W. Esposito 1990. A numerical model of the uranian dust rings. *Icarus* **86,** 530–560.

Cuzzi, J. N. 1985. Rings of Uranus: Not so thick, no so black. *Icarus* **63,** 312–316.

Cuzzi, J. N., and R. H. Durisen 1990. Bombardment of planetary rings by meteoroids: General formulation and effects of Oort cloud projectiles. *Icarus* **84,** 467–501.

De Pater, I., M. R. Showalter, J. J. Lissauer, and J. R. Graham 1996. Keck infrared observations of Saturn's E and G rings during Earth's 1995 ring plane crossings. *Icarus* **121,** 195–198.

Draine, B. T. 1988. The discrete-dipole approximation and its application to interstellar graphite grains. *Astrophys. J.* **333,** 848–872.

Esposito, L. W., and J. E. Colwell 1989. Creation of the Uranus rings and dust bands. *Nature* **339,** 605–607.

Esposito, L. W., J. N. Cuzzi, J. B. Holberg, E. A. Marouf, G. L. Tyler, and C. C. Porco 1984. Saturn's rings—Structure, dynamics, and particle properties, in *Saturn* (T. Gehrels and M. S. Matthews, Eds.), Univ. of Arizona Press, Tucson, pp. 463–545.

Estrada, P. R., and J. N. Cuzzi 1996. Voyager observations of the color of Saturn's rings. *Icarus* **122,** 251–272.

French, R. G., J. Cuzzi, L. Dones, and J. Lissauer 1997. High-resolution imaging of Saturn's G ring from the Hubble Space Telescope. *Bull. Am. Astron. Soc.* **29,** 1097.

Goody, R. M., and Y. L. Yung 1989. *Atmospheric Radiation: Theoretical Basis*, 2nd ed. Oxford Univ. Press, Cambridge.

Greenberg, R., J. F. Wacker, W. K. Hartmann, and C. R. Chapman 1978. Planetesimals to planets: Numerical simulation of collisional evolution. *Icarus* **35,** 1–26.

Grün, E., H. A. Hook, H. Fechtig, and R. H. Geise 1985. Collisional balance of the meteoritic complex. *Icarus* **62,** 244–272.

Grün, E., G. R. Morfill, and D. A. Mendis 1984. Dust-magnetosphere interactions. In *Planetary Rings* (R. Greenberg and A. Brahic, Eds.), pp. 200–272. Univ. of Arizona Press, Tucson.

Gurnett, D. A., E. Grün, D. Gallagher, W. S. Kurth, and F. L. Scarf 1983. Micron-sized particles detected near Saturn by the Voyager Plasma Wave Instrument. *Icarus* **53,** 236–254.

Hamilton, D. P., and J. A. Burns 1994. Origin of Saturn's E ring: Self-sustained, naturally. *Science* **264,** 550–553.

Hansen, J. E., and L. D. Travis 1974. Light scattering in planetary atmospheres. *Spac. Sci. Rev.* **16,** 527–610.

Holland, A. C., and G. Gagne 1970. The scattering of polarized light by polydisperse systems of irregular particles. *Appl. Opr.* **9,** 1113–1121.

Hood, L. L. 1989. Investigation of the Saturn dust environment from the analysis of energetic charged particle measurements. *Cassini AO* **13.**

Johnson, R. E., L. A. Barton, J. W. Boring, W. A. Jesser, W. L. Brown, and L. J. Lanzerotti 1985. Charged particle modification of ices in the saturnian and jovian systems. In *Ices in the Solar System* (J. Klinger *et al.*, Eds.), NATO ASI Series **156,** pp. 301–315. D. Reidel, Boston.

Kendall, J. 1978. The impossibility of comminuting small particles by compression. *Nature* **272,** 710–711.

Khare, V., and H. M. Nussenzveig 1977. Theory of the glory. *Phys. Rev. Lett.* **38,** 1279–1282.

Liou, K. N., Q. Cai, J. B. Pollack, and J. N. Cuzzi 1983. Light scattering by randomly oriented cubes and parallelepipeds. *Appl. Opt.* **22,** 3001–3008.

Lissauer, J. J., and V. S. Safronov 1991. The random component of planetary rotation. *Icarus* **93,** 288–297.

Mayer, E., and R. Pletzer 1986. Astrophysical implications of amorphous ice—A microporous solid. *Nature* **319,** 298–301.

McGuire, A. F., and B. W. Hapke 1995. An experimental study of light scattering by large, irregular particles. *Icarus* **113,** 134–155.

Mekler, Y., and M. Podolak 1994. Formation of amorphous ice in the protoplanetary nebula. *Planet. Space Sci.* **42,** 165–870.

Meyer-Vernet, N., A. Lecacheux, and B. M. Pedersen 1997. Constraints on Saturn's G ring from the Voyager 2 radio astronomy instrument. *Icarus*, in press.

Mishchenko, M. I., and A. Macke 1997. Asymmetry parameters of the phase function for isolated and densely packed spherical particles with multiple internal inclusions in the geometric optics limit. *J. Quant. Spectrosc. Radiat. Transfer* **57,** 767–800.

Mishchenko, M. I., and J. M. Dlugach 1992. Can weak localization of photons explain the opposition effect of Saturn's rings? *Mon. Not. R. Astron. Soc.* **254,** 15P–18P.

Mishchenko, M. I., L. D. Travis, R. A. Kahn, and R. A. West 1997. Modeling phase functions for dust-like tropospheric aerosols using a shape mixture of randomly oriented polydisperse spheroids. *J. Geophys. Res.* **102,** 13,543–13,553.

Mishchenko, M. I., L. D. Travis, and A. Macke 1996. Scattering of light by polydisperse, randomly oriented, finite circular cylinders. *Appl. Opt.* **35,** 4927–4940.

Moore, M. H., and R. L. Hudson 1992. Far-infrared spectral studies of phase changes in water ice induced by proton irradiation. *Astrophys. J.* **401,** 353–360.

Morfill, G., E. Grün, and T. V. Johnson 1983. Saturn's E, G, and F rings: modulated by the plasma sheet? *J. Geophys. Res.* **88,** 5573–5579.

Munionen, K. 1994. Coherent backscattering by Solar System dust particles. In *IAU Symposium 160: Asteroids, Comets, Meteors. 1994*, pp. 271–296. Lunar and Planetary Inst., Houston.

Muinonen, K., K. Lumme, J. Peltoneimei, and W. Irvine 1989. Light scattering by randomly oriented crystals. *Appl. Opt.* **28,** 3051–3060.

Muinonen, K., T. Nousiainen, P. Fast, K. Lumme, and J. Peltoneimi 1996. Light scattering by Gaussian random particles: ray optics approximation. *J. Quant. Spectrosc. Radiat. Transfer* **55,** 577–601.

Nicholson, P. D., M. R. Showalter, L. Dones, R. G. French, S. M. Larson, J. J. Lissauer, C. A. McGhee, P. Seitzer, B. Sicardy, and G. E. Danielson 1996. Observations of Saturn's ring-plane crossing in August and November 1995. *Science* **272,** 509–515.

Northrop, T. G., and T. J. Birmingham 1990. Plasma drag on a dust grain due to Coulomb collisions. *Planet. Space Sci.* **319,** 319–326.

Pollack, J. B., and J. N. Cuzzi 1980. Scattering by nonspherical particles of size comparable to a wavelength: A new semi-empirical theory and its application to tropospheric aerosols. *J. Atmos. Sci.* **37,** 868–881.

Richardson, J. D. 1995. An extended plasma model for Saturn. *Geophys. Res. Lett.* **22,** 1177–1180.

Schmitt, B., J. Ocampo, and J. Klinger 1987. Structure and evolution of different ice surfaces at low temperature absorption studies. *J. Phys. Suppl. 3,* **48,** 519–525.

Schmitt, B., S. Espinasse, R. J. A. Grin, J. M. Greenberg, and J. Klinger 1989. Laboratory studies of cometary ice analogues. *ESA SP* **302,** 65–69.

Showalter, M. R. 1996. Saturn's D ring in the Voyager images. *Icarus* **124,** 277–689.

Showalter, M. R., and J. N. Cuzzi 1993. Seeing ghosts: Photometry of Saturn's G ring. *Icarus* **103,** 124–143.

Showalter, M. R., J. A. Burns, J. N. Cuzzi, and J. B. Pollack 1987. Jupiter's ring system: New results on structure and particle properties. *Icarus* **69,** 458–498.

Showalter, M. R., J. N. Cuzzi, and S. M. Larson 1991. Structure and particle properties of Saturn's E ring. *Icarus* **94,** 451–473.

Showalter, M. R., J. B. Pollack, M. E. Ockert, L. R. Doyle, and J. B. Dalton 1992. A photometric study of Saturn's F ring. *Icarus* **100,** 394–411.

Strazzulla, G., L. Torrisi, and G. Foti 1988. Light scattering from ion-irradiated frozen gases. *Europhys. Lett.* **7,** 431–434.

Tsintikidis, D., D. Gurnett, L. J. Granroth, S. C. Allendorf, and W. S. Kurth 1994. A revised analysis of micron-sized particles detected near Saturn by the Voyager 2 plasma wave instrument. *J. Geophys. Res.* **99**(A2), 2261–2270.

van de Hulst, H. C. 1957. *Light Scattering by Small Particles*. Dover Publications, New York, NY. [Reprinted 1981]

Warren, S. G. 1984. Optical constants of ice from the ultraviolet to the microwave. *Appl. Opt.* **23,** 1206–1225.

Waterman, P. C. 1971. Symmetry, unity, and geometry in electromagnetic scattering. *Phys. Rev. D* **3,** 825–839.

Zerull, R. H., and R. H. Geise 1974. Microwave analogue studies, in *Planets, Stars, and Nebulae Studied with Photopolarimetry* (T. Gehrels, Ed.), pp. 901–914. Univ. of Arizona Press, Tucson.